FISEVIER

Contents lists available at ScienceDirect

Applied Energy

journal homepage: www.elsevier.com/locate/apenergy



A high-performance intermediate temperature reversible solid oxide cell with a new barrier layer free oxygen electrode

Kai Zhao a, 1, Jiaxin Lu a, Long Le b, Chris Coyle b, Olga A. Marina b, a, Kevin Huang a, a

- ^a Department of Mechanical Engineering, University of South Carolina, Columbia, SC 29201, United States of America
- ^b Energy and Environment Directorate, Pacific Northwest National Laboratory, Richland, WA99352, USA

ARTICLE INFO

Keywords: Reversible solid oxide cell Oxygen electrode Barrier layer free design Oxygen reduction and evolution reactions

ABSTRACT

The best solution to address the critical durability issue of solid oxide electrolytic cells (SOECs) for high-efficiency and high-rate $\rm H_2$ production is to lower the operating temperature without sacrificing the performance. Developing high performance oxygen electrodes (OEs) is a key to capitalizing this solution. Here we report on a highly active OE for intermediate temperature $\rm ZrO_2$ -based SOECs without a $\rm CeO_2$ barrier layer. The new barrier-layer-free (BLF) OE is a composite of two materials, $\rm (Bi_{0.75}Y_{0.25})_{0.93}\rm Ce_{0.07}O_{1.5\pm\delta}$ (BYC) that exhibits high oxide-ion conductivity and $\rm La_{0.8}\rm Sr_{0.2}\rm MnO_3$ (LSM) that possesses a high electronic conductivity to enable fast oxygen reduction/evolution reactions (ORR/OER). Featuring a microscale porous BYC scaffold decorated with high surface area LSM nanoparticles (NPs), the new BLF-OE exhibited a low area specific resistance (ASR) of 0.10 $\rm \Omega$ cm² at 650 °C in air. With 50%H₂–50%H₂O as a feed to hydrogen electrode (HE) and air to OE, the single cell performance achieved 588 mA cm² at 0.80 V in the fuel cell mode and 688 mA cm² at 1.30 V in the electrolytic mode at 650 °C. Our in-house testing showed that this level of performance was ~3.5 × higher than the cell with the benchmark $\rm La_{0.6}\rm Sr_{0.4}\rm Co_{0.2}\rm Fe_{0.8}\rm O_{3.8}\text{-Ce}_{0.9}\rm Gd_{0.1}\rm O_{2.5}$ OE. The long-term durability testing under alternating fuel cell and electrolytic modes showed a low degradation rate of 0.10 mA cm² h¹ over 550 h. These encouraging results showed the great promise of the newly developed BYC-LSM to be an excellent OE candidate for intermediate temperature SOECs.

1. Introduction

Reversible solid oxide cells (RSOCs) are a class of advanced electrochemical devices that find extensive applications in clean and efficient power generation and chemical conversion. RSOCs can operate in two modes: (1) solid oxide fuel cell (SOFC) mode, which converts chemical energy in fuels into electricity, and (2) solid oxide electrolytic cell (SOEC) mode, which produces chemicals through electrolysis using electrical energy and chemical feedstocks [1-3]. The state-of-the-art RSOCs consist of a Ni-yttria-stabilized zirconia (YSZ) hydrogen electrode (HE) support, HE functional layer, YSZ electrolyte, gadolinium doped ceria (GDC) barrier layer, and La_{0.6}Sr_{0.4}Co_{0.2}Fe_{0.8}O₃₋₈-GDC oxygen electrode (OE) [1,4,5], for the reversible operation. The use of ceramic electrolytes and solid electrodes requires higher operating temperatures to achieve high ionic conductivity and fast charge transport kinetics [1]. Unfortunately, high operating temperatures impose challenges to the durability and cost of RSOC systems [3,4,6]. Therefore, a technical solution to address the durability and cost issues is to lower

the operating temperature, preferably to the intermediate temperature (IT) range (e.g., 600–700 °C). As the operating temperature is reduced, however, the performance of RSOC is suppressed, particularly due to slower OE kinetics [7–9]. Improving OE performance has, therefore, become a key to enabling IT-RSOCs toward commercialization.

Over the past decades, extensive research has been conducted on mixed oxide-ion and electron conducting perovskite oxides as potential OEs for IT-RSOCs. Among them, lanthanum-cobalt-based perovskites (e.g., $La_{1-x}Sr_xCo_{1-y}Fe_yO_{3-\delta}$ (LSCF)) and double perovskites (e.g., $Pr_{1+x}Ba_{1-x}Co_2O_{5+\delta})$ have received significant attention due to their high mixed conductivity and excellent electrocatalytic activity for ORR/OER [7–11]. However, these materials are subject to either phase transformation-induced degradation or incompatible thermal expansion coefficients (TECs) with YSZ electrolytes [8] at elevated temperatures. Moreover, chemical reactions between YSZ and LSCF occur at high temperatures, invoking insulating and deleterious phases such as La_2ZrO_7 and $SrZrO_3$, which negatively impact the electrochemical performance [10]. To mitigate this issue, a thin barrier layer, such as

https://doi.org/10.1016/j.apenergy.2024.122962

Received 1 December 2023; Received in revised form 20 January 2024; Accepted 1 March 2024 0306-2619/© 20XX

^{*} Corresponding authors.

E-mail addresses: Olga.Marina@pnnl.gov (O.A. Marina), huang46@cec.sc.edu (K. Huang).

¹ Present Address: School of Materials Science and Hydrogen Energy, Foshan University, Foshan 528000, People's Republic of China

doped CeO_2 , is commonly applied between the OE and the electrolyte to prevent the detrimental reactions and electrode delamination [12,13]. Unfortunately, at reduced temperatures (\leq 650 °C), the barrier layer itself exhibits significant ohmic resistance, further reducing the electrochemical performance. Therefore, the development of high-performance OEs without barrier layer at the electrolyte interface is critical

Recently, a class of composite materials consisting of $\rm La_{0.8}Sr_{0.2}MnO_3$ (LSM) and stabilized $\rm Bi_2O_3$ has been identified as a potential OEs for IT-RSOCs [14,15]. In this design, LSM serves as an electronic conductor, while providing excellent structural and chemical compatibility with zirconia-based electrolytes [16,17]. The stabilized $\rm Bi_2O_3$ are the best oxide-ion conductors ever known to the RSOC community [12]. Through an appropriate doping of Ce and Y into $\rm Bi_2O_3$ (BYC), our early studies have demonstrated that it can retain its cubic phase and high oxide-ion conductivity for extended SOFC operation in the IT-range [15,18,19]. In addition, it shows good chemical compatibility with LSM and ScSZ at the operating temperature (see Fig. S2 and the corresponding discussion in SI). Therefore, BYC-LSM composite has been considered as a logical choice for IT-RSOCs.

Electrochemical performances of other stabilized Bi $_2O_3$ /LSM composite OEs for RSOC have been previously reported [20–25]. The observations are rather clear, i.e., the high oxide-ion conductivity of stabilized Bi $_2O_3$ significantly accelerates the kinetics of ORR/OER and reduces the ORR/OER ASR. For example, the ASR of a yttria stabilized bismuth oxide (YSB)-LSM OE on an YSZ electrolyte is \sim 0.10 Ω cm 2 at 700 °C [22], which is 30% lower than that of the conventional LSCF-GDC OE [26]. When implemented in single cells, the electrolysis current density of the YSB-LSM is \sim 50% higher than that with LSCF-GDC OE at 1.30 V [21].

Additionally, the electrochemical activity of the composite electrode is strongly dependent on its microstructure and is influenced by the fabrication processes [23]. A rational electrode design that incorporates well-connected oxide-ion conduction channels (such as BYC backbones) and electronic conduction pathways (such as connected LSM nanoparticles (NPs)) could be another way to enhance the ORR/OER kinetics by increasing triple phase boundaries (TPBs). However, there is still a lack of knowledge if such an oxide-ion conductor scaffold decorated with electron conductive NPs is stable over a long-term operation under IT condition.

In this work, we show the electrochemical performances of LSM-NPs decorated BYC scaffold as a BLF OE in both symmetrical cell and full cell configurations and compare with screen-printed BYC-LSM and baseline LSCF-GDC counterparts. Long-term stability of the cell performance was investigated under alternating SOFC and SOEC operating modes and the stability-microstructure relationship was established by post-test microstructural analysis.

2. Experimental procedure

2.1. Materials synthesis

The LSM and BYC powders were both synthesized by the citric acid-nitrate method [14,15]. For the LSM powder, stoichiometric amounts of metal nitrates and citric acid were dissolved into de-ionized water. The molar ratio of the citric acid to total metal ions was 2.0:1.0. The solution was then heated in an oven at 250 °C for auto ignition and self-sustained combustion. The resulting ash was collected and subsequently calcined at 900 °C for 5 h in air. The BYC powder was synthesized in a similar way except that the nitrates were dissolved into 1.3 mol L^{-1} nitric acid and the molar ratio of citric acid to total metal ions was adjusted to 1.5:1.0. The collected powers were calcined at 700 °C for 4 h in air to obtain a pure phase [14].

2.2. Fabrication of symmetrical cells

The two-electrode symmetrical cells consisting of BYC-LSM OE, $(Sc_2O_3)_{0.1}(CeO_2)_{0.01}(ZrO_2)_{0.89}$ (ScSZ) electrolyte membrane and Ag counter electrode were fabricated through the dry-pressing and screen-printing processes. The ScSZ powder (Daiichi Kigenso Kagaku Co. Ltd., Japan) was dry pressed into a disk pellet with a diameter of 20 mm and a thickness of 1.2 mm at a pressure of 60 MPa, followed by sintering at 1400 °C for 5 h in air to achieve high density. The BYC-LSM OE was fabricated on the ScSZ electrolyte membrane by two processes:

Process-1 (screen-printing): The screen-printing paste was prepared by intimately mixing 60 wt% LSM and 40 wt% BYC with a binder vehicle (V-006 A, Heraeus, US) at a solid loading of 50 wt%. The paste was then screen-printed on surfaces of the ScSZ electrolyte. The printing process was repeated six times after drying at 80 °C each time to achieve a thickness of $\sim\!30~\mu m$. The printed BYC-LSM electrode was finally calcined at 800 °C for 2 h. The electrode fabricated in this way is referred to as BYC-LSM(Mix).

Process-2 (infiltration): A screen-printing paste was prepared by mixing 77 wt% BYC, 23 wt% pore former (carbon black, Chemical-Store, US), and V-006 A binder vehicle at a solid content of 50 wt%. The paste was screen-printed onto surfaces of the ScSZ electrolyte in the same way as described above. The electrode was calcined at 800 °C for 2 h to form a porous BYC skeleton. The LSM NPs were then incorporated into the BYC skeleton by vacuum-assisted nitrate solution infiltration. The LSM precursor solution was prepared by dissolving stoichiometric amounts of metal nitrates into the de-ionized (DI) water, with a total metal concentration of 0.4 mol L⁻¹. The infiltration was repeated 15 times to achieve a \sim 25 wt% LSM loading in the BYC skeleton. Finally, the BYC-LSM electrode was calcined at 700 °C for 2 h in air to decompose the nitrates and form LSM phase. The resulting electrode is referred to as BYC-LSM(Infil).

2.3. Fabrication of single cells

HE-supported thin film ScSZ electrolyte single cells with Ni-(Y₂O₃)_{0.04}(ZrO₂)_{0.96} (denoted as Ni-4YSZ) as the support, Ni-ScSZ as the HE functional layer, and BYC-LSM as the OE were fabricated by a combination of phase inversion, spin-coating, screen printing and infiltration processes [15,27,28]. For the HE support, a phase inversion process was used, which is described as follows. A slurry was first prepared by thoroughly mixing 60 wt% NiO and 40 wt% 4YSZ powder with a solvent binder system consisting of polyethersulfone (PESF, Amerco Performance Radel A-300), polyvinylpyrrolidone (Sigma-Aldrich), and 1-Methyl-2-Pyrrolidone (Sigma-Aldrich). The slurry was then cast on a glass plate, followed by immersing into DI water for the solvent exchange. The resulting NiO-4YSZ green tape was punched into disk-shaped samples with a diameter of 32 mm, followed by calcining at 1000 °C for 3 h to burn out organics. Next, NiO-ScSZ functional layer and ScSZ electrolyte layer were sequentially deposited on the surface of NiO-4YSZ support by spin-coating. The multilayer structure was subsequently sintered at 1400 °C for 4 h in air to achieve a dense electrolyte membrane. Finally, two different types of BYC-LSM OEs were fabricated by screen printing and infiltration processes on the surface of ScSZ electrolyte, using the same procedures described in section 2.2. The active surface area of OE was 1.30 cm2. The single cell with the conventional $La_{0.6}Sr_{0.4}Co_{0.2}Fe_{0.8}O_{3-\delta}$ (LSCF)- $Ce_{0.9}Gd_{0.1}O_{1.95}$ (GDC) OE was fabricated as well for comparison purpose. The details are described in the SI.

2.4. Electrochemical performance evaluations

The electrochemical properties of the BYC-LSM electrodes in a symmetrical cell configuration were first evaluated using electrochemical impedance spectroscopy (EIS) method. A silver mesh/wire was used as

the current collector. EIS spectra were collected using a Solartron electrochemical workstation consisting of 1470 multichannel potentiostat and 1255B frequency response analyzer.

The performance of the HE-supported single cell was evaluated by a lab-designed single cell test setup consisting of a single cell sample holder, a tubular furnace, and a set of mass flow controllers (Alicat Scientific). Steam was created in the hot zone in situ by burning hydrogen. The steam concentration was verified by the open-circuit voltage (OCV) measurements and compared to that predicted by the Nernst equation.

The microstructure and elemental distribution of the single cells were analyzed using a JEOL IT500HR Field Emission (FE) scanning electron microscope (SEM) equipped with dual 100 mm² energy dispersive spectroscopy (EDS) detectors.

3. Results and discussion

3.1. Microstructure of BYC-LSM

The microstructures and EDS elemental mapping of the two types of BYC-LSM electrodes prepared before testing are shown in Fig. 1. Both OEs exhibit porous microstructures and uniform elemental distribu-

tions on the dense ScSZ electrolyte. In particular, the BYC-LSM(Mix) OE shows well-connected grains of two phases, see Fig. 1(a)-(c), with an average grain size of $\sim\!510$ nm estimated by image analysis techniques [29] (the detailed results can be found in Fig. S6(a) and Fig. S6(c) in the supplementary material (SI)). In the case of the BYC-LSM(Infil) OE, Fig. 1(d)-(f) show abundant nanoparticles (NPs) on the walls of BYC porous skeleton. The EDS mapping confirms that these NPs are LSM (see La mapping; other elements are shown in Fig. S8 in the SI). The average size of LSM NPs is $\sim\!45$ nm (see Fig. S6(b) and Fig. S6(d) in the SI). Evidently, the BYC-LSM(Infil) OE has more TPBs than its BYC-LSM(Mix) counterpart, implying higher performance.

3.2. Electrochemical properties of BYC-LSM symmetrical cell

The electrochemical properties of the two types of BYC-LSM OEs were comparatively investigated by EIS; the results are shown in Fig. 2 (a). To highlight the difference in electrode's ASR, the ohmic resistance was subtracted from the spectra [30]. As expected, ASR of the BYC-LSM (Infil) is much lower than its BYC-LSM(Mix) counterpart. To assist in the analysis of identifying the improved process, we employed Distribution Relaxation Times (DRT) method [31]. Fig. 2 (b) shows the corre-

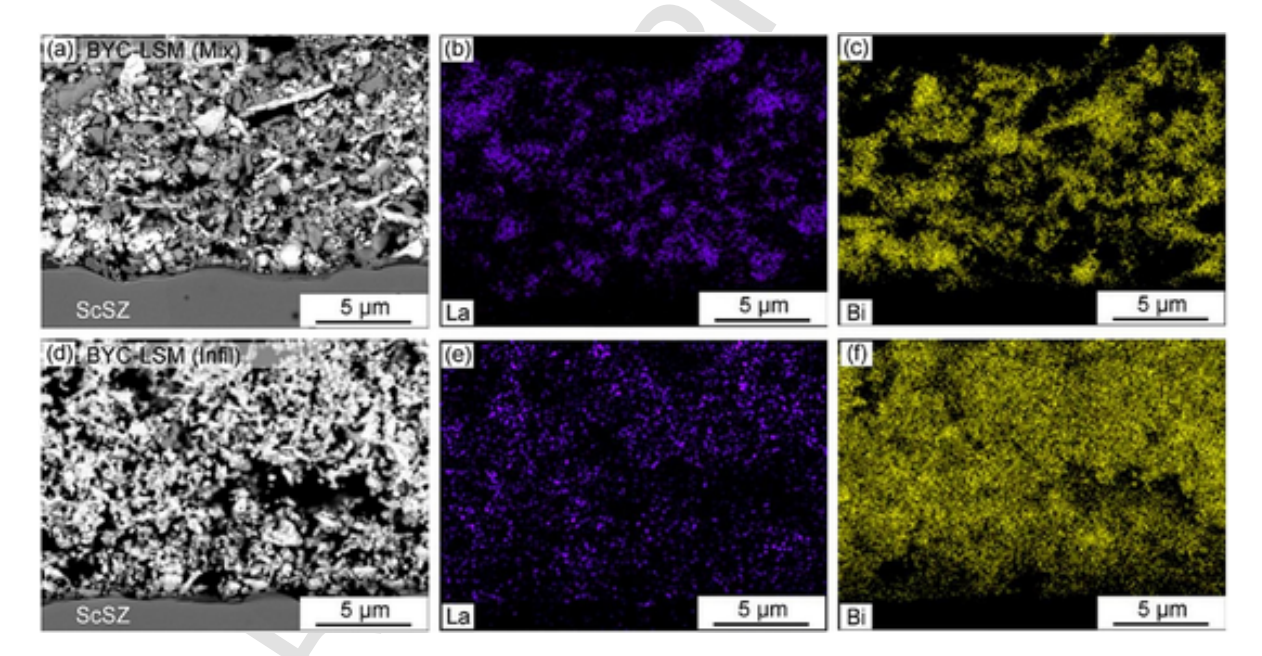


Fig. 1. Cross-sectional SEM images of BYC-LSM electrode. (a) - (c) BYC-LSM(Mix) electrode and the elemental mapping for La and Bi; and (d) - (f) BYC-LSM(Infil) electrode and the elemental mapping for La and Bi.

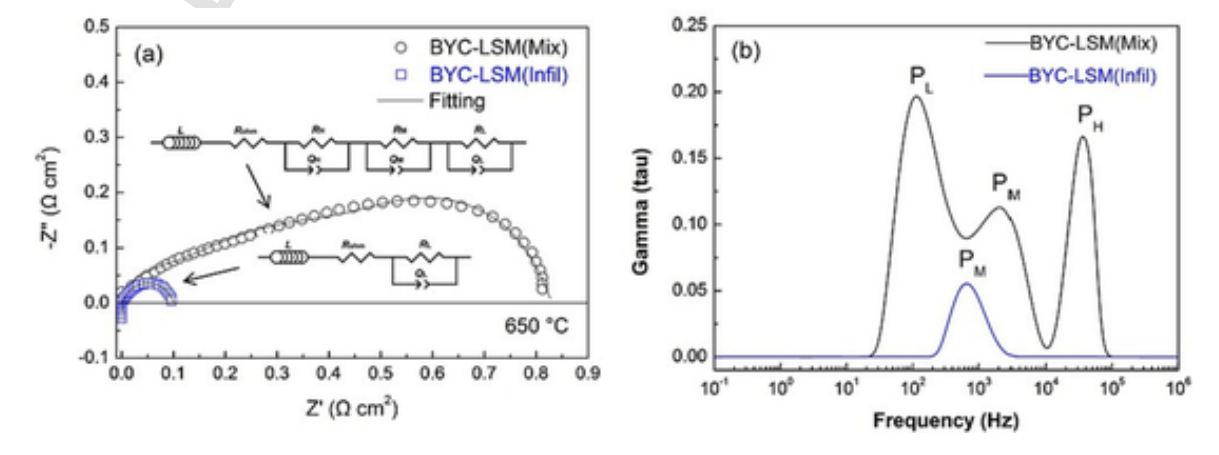


Fig. 2. (a) Nyquist plots of BYC-LSM electrodes and (b) the corresponding DRT profiles (P_H: high frequency peak, P_M: medium frequency peak, and P_L: low frequency peak).

sponding DRT profiles of Fig. 2 (a). For BYC-LSM(Mix), DRT profile reveals three distinct peaks at high frequency range over 10^4 – 10^5 Hz, medium range over 10^3 – 10^4 Hz and low range over 10^1 – 10^2 Hz, respectively.

In comparison, BYC-LSM(Infil) displays a very different DRT profile, in which the high frequency peak ($P_{\rm H}$) disappears, while the medium and low frequency peaks are merged into a single peak. The disappearance of $P_{\rm H}$ suggests that BYC-LSM(Infil) has a fast charge transfer process, and the rate-limiting step is likely the surface adsorption/dissociation/ diffusion of oxygen molecules/atoms. This is the result of using a highly oxide-ion conductive BYC phase and high-surface-area electronically conductive LSM phase. As the area under each DRT peak is proportional to the polarization ASR of a specific electrochemical process [32,33], the reduced peak area in the BYC-LSM(Infil) implies a lower ASR than BYC-LSM(Mix), which is consistent with Fig. 2(a).

Based on the results obtained from the initial DRT analysis, all impedance data were further fitted by the $LR_{\rm ohm}(R_{\rm H}Q_{\rm H})(R_{\rm M}Q_{\rm M})(R_{\rm L}Q_{\rm L})$ and $LR_{\rm ohm}(R_{\rm L}Q_{\rm L})$ equivalent circuit models, respectively, see the inset of Fig. 2 (a). The $(R_{\rm H}Q_{\rm H})$, $(R_{\rm M}Q_{\rm M})$ and $(R_{\rm L}Q_{\rm L})$ represent high-, intermediate-and low-frequency impedance responses, respectively. The characteristic electrochemical parameters, such as equivalent capacitance C and relaxation frequency f are calculated by the following equations [34–36]:

$$C = (R \cdot Q)^{1/n} / R \tag{1}$$

$$f = (R \cdot Q)^{-1/n} / (2\pi) \tag{2}$$

where, R is resistance, Q is constant phase element and n is an exponential parameter, which can be obtained from the fittings. The values of chi-squared function (χ^2) are a measure of goodness of fit and are on the orders of magnitude of 10^{-3} – 10^{-4} , indicating a good fit between experimental impedance data and models. The fitting results are summarized in Table 1.

The obtained equivalent capacitance C and relaxation frequencies (f) provide insights into the electrochemical processes. The high-frequency impedance response, characterized by a capacitance of $\sim 10^{-6}$ F cm⁻² and a relaxation frequency of $\sim 10^{5}$ Hz, is an indicative of the charge transfer process occurring at the electrode/electrolyte interface [35]. On the other hand, the intermediate- and low-frequency impedance arcs are featured with characteristic capacitances on the orders of magnitude of 10^{-4} and 10^{-3} F cm⁻², along with relaxation frequencies of 10^{3} and 10^{2} Hz, respectively. These values correspond to the intermediate ($P_{\rm M}$)- and low-frequency ($P_{\rm L}$) peaks in the DRT profiles as shown in Fig. 2 (b), which can be attributed to the surface oxygen exchange processes, including oxygen adsorption, dissociation, and diffusion on the surface of a porous electrode [35–37].

The ASR from the high-frequency charge transfer process ($R_{\rm H}$) determined from the fitting is 0.17 Ω cm² for BYC-LSM(Mix). However, this impedance response disappears in BYC-LSM(Infil). The absence of a charge transfer resistance in BYC-LSM(Infil) implies that BYC-LSM (Infil) possesses an excellent electrocatalytic activity toward oxygen redox reactions, which could be a combined result of abundant LSM NPs ensuring high triple phase boundary (TPB) density and strong bonding with ScSZ electrolyte [38,39].

The ASR of the mid-to-low frequency surface oxygen exchange process $(R_{\rm M}+R_{\rm L})$ is 0.77 Ω cm² for BYC-LSM(Mix) vs. 0.10 Ω cm² for

BYC-LSM(Infil). This difference is likely attributed to the density of TPBs in the two electrodes. From Fig. S6 in SI, BYC-LSM(Mix) is seen with an average grain size of ~510 nm vs. ~45 nm of LSM in BYC-LSM (Infil). The high specific surface area of LSM increases TPB density and lowers ASR associated with the surface oxygen exchange process ($R_{\rm M}+R_{\rm L}$) and charge transfer process occurring at TPBs [40]. The total ASR of BYC-LSM(Infil) electrode is only 0.10 Ω cm² at 650 °C, which is superior to the benchmark La_{0.6}Sr_{0.4}Co_{0.2}Fe_{0.8}O_{3-δ} (LSCF) electrodes even with modified electrode surface (ASR varies from 0.12 to 1.00 Ω cm² at 650 °C) [38,40,41].

3.3. Electrochemical performance of single cells

The initial V-I curves of single cells with the two types of BLF-OEs operated under air and 50% H₂–50% H₂O at 650 °C are shown in Fig. 3. For comparison, the V-I curve of the same type of cell but with the LSCF-GDC OE is also included. The three single cells exhibit similar open-circuit voltages (OCVs) of 0.98 V, which is close to the theoretical value (0.99 V) for air vs. 50% H₂-50% H₂O [42]. It indicates excellent gas tightness of all cells and accurate steam concentration. At 0.80 V of the fuel cell mode, the cell with BYC-LSM(Infil) OE shows a current density of 588 mA cm⁻², which is nearly twice the current density of BYC-LSM(Mix) (300 mA cm⁻²) and over four times the current density of LSCF-GDC (140 mA cm⁻²). Similarly, in the electrolysis mode, the cell with BYC-LSM(Infil) OE exhibits an electrolysis current density $\sim 2 \times$ BYC-LSM(Mix) and $\sim 3.5 \times$ LSCF-GDC at 1.30 V. These results are consistent with the ASRs shown in Fig. 2. The fact that BLF-OEs significantly outperform LSCF-GDC not only demonstrates their great potential for IT-RSOCs, but also the importance to eliminate OE's barrier layer to simplify fabrication process and achieve better performance. The latter is one of the reasons why CeO2-based barrier layer free OEs and proton conducting SOCs with highly oxygen-active OEs generally have higher performance than ZrO₂-based counterparts at IT-

Electrochemical impedance spectra of these three single cells were also analyzed under three different operating conditions: OCV, fuel cell mode (at 0.80 V), and electrolysis mode (at 1.30 V). Fig. 4 shows the corresponding Nyquist plots and DRT profiles. Note that the EIS spectra collected from single cells include electrochemical processes in both OEs and HEs. As the cells have an identical, HE and electrolyte, the difference in resistances shall be originated from OEs. The ohmic ($R_{\rm ohm}$) and polarization ($R_{\rm p}$) resistances of the single cells are determined from the impedance spectra fittings, and the detailed fitting results are listed in Table S1 in the SI.

Extracted from Fig. 4, Fig. 5 shows the variation of $R_{\rm ohm}$ and $R_{\rm p}$ of all three types of single cells vs. operating conditions. Evidently, cell loading condition does not affect $R_{\rm ohm}$, but alters $R_{\rm P}$. It is interesting to see that $R_{\rm p}$ is higher for electrolysis mode and lower for fuel cell mode than that for OCV. Among the three cells, the BYC-LSM(Infil) cell clearly exhibited a lower $R_{\rm ohm}$ than the BYC-LSM(Mix) and LSCF-GDC cells. One reason could be the sheet resistance related to the electronic conductivity of the OE [43,44]. The sheet resistance of BYC-LSM(Infil) measured at 650 °C in air is 1.52 Ω sq.-1, which is only 3% of 56.5 Ω sq.-1 for BYC-LSM(Mix). All sheet resistance data are shown in Fig. S4 in the SI. In addition, compared to BYC-LSM(Mix) OE, the improved bonding between BYC and ScSZ in the BYC-LSM(Infil) OE further facilitates the re-

 Table 1

 Electrochemical parameters obtained from impedance spectra fittings.

Electrode	$R_{\rm H}$ (Ω cm ²)	C _H (F cm ⁻²)	f _H (Hz)	$R_{ m M}$ (Ω cm ²)	C _M (F cm ⁻²)	$f_{ m M}$ (Hz)	$R_{\rm L}$ (Ω cm ²)	C _L (F cm ⁻²)	f _L (Hz)	$R_{\rm p}$ (Ω cm ²)
BYC-LSM (Mix)	0.17	4.32×10^{-6}	2.10×10^5	0.51	1.74×10^{-4}	1.78×10^3	0.26	5.18×10^{-3}	120	0.94
BYC-LSM (Infil)	-	-	-	-	-	-	0.10	2.70×10^{-3}	586	0.10

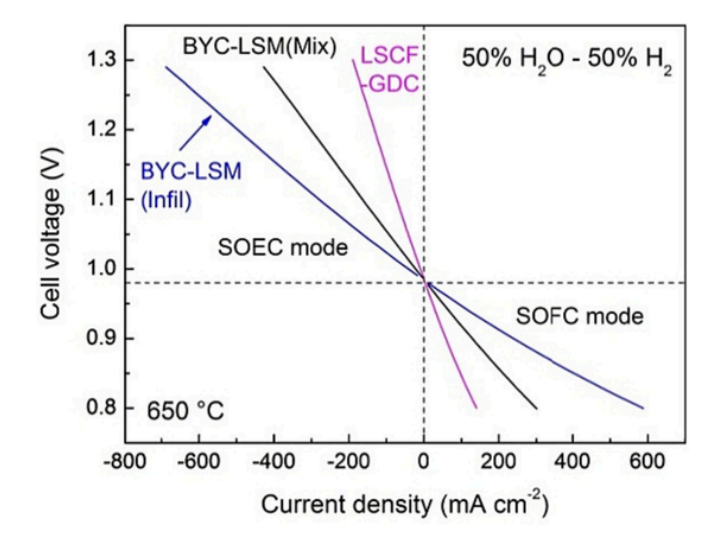


Fig. 3. Current-voltage curves of single cells with BYC-LSM(Mix), BYC-LSM (Infil) and LSCF-GDC electrodes, respectively, at 650 $^{\circ}$ C.

duction of the ohmic resistance. The much higher $R_{\rm ohm}$ of the LSCF-GDC cell is very likely resulted from the GDC barrier layer for the same ScSZ electrolyte.

The polarization ASR (R_p) of BYC-LSM(Infil) OE is also lower than BYC-LSM(Mix) under OCV, SOFC and SOEC modes, indicating its higher electrocatalytic activity for ORR than for OER. To understand the individual electrochemical process involved in R_p , we extract equivalent capacitance and relaxation frequency data from the fittings; they

are listed in Table S1 in SI. For the high frequency peak on the DRT plot, an equivalent capacitance of 10^{-4} F cm⁻² and a relaxation frequency of 10^3 Hz suggest that the corresponding resistance ($R_{\rm H}$) is related to charge transfer process [33,45]. For the intermediate and low frequency peaks, an equivalent capacitance of 10^{-2} — 10^1 F cm⁻² and a relaxation frequency of 10^{-1} — 10^2 Hz imply that the corresponding resistances ($R_{\rm M}$ and $R_{\rm L}$) could be resulted from dissociative adsorption and diffusion-related processes [33,45,46].

Fig. 6 further plots deconvoluted R_p in different frequency domains. It shows that $R_{\rm H}$ of BYC-LSM(Mix) cell decreases from 0.38 (at OCV) to $0.27~\Omega~cm^2$ (at 0.80~V) under the fuel cell mode. This reduction suggests an accelerated charge transfer kinetics, which is well expected from Butler-Volmer equation, and is consistent with previous works on BYC-LSM and other perovskite type OEs [15,47]. Meanwhile, $R_{\rm M}+R_{\rm L}$ shows no obvious variations (0.11- 0.12 Ω cm²) between the two modes. The overall electrode polarization ($R_p = R_H + R_M + R_L$) decreases from 0.50 Ω cm² under OCV to 0.38 Ω cm² under fuel cell mode. When it was switched from OCV to electrolysis mode, charge transfer resistance (RH) exhibits a similar reduction trend, while $R_{\rm M}+R_{\rm L}$ increases from 0.12 to 0.42 Ω cm². According to our previous work, polarization resistance of BYC-LSM should decrease with DC bias (overpotential) in both fuel cell and electrolysis mode [15]. The increased $R_{\rm M}$ + $R_{\rm L}$ could be related to HE, e.g., increased diffusion resistance from the fuel electrode [42,48]. More work is needed to verify this hypothesis. Nevertheless, the higher $R_{\rm p}$ under SOEC mode signals that SOEC would underperform compared to SOFC mode.

Compared to the BYC-LSM(Mix) cell, $R_{\rm p}$ of the BYC-LSM(Infil) cell is reduced by 40, 50 and 25%, respectively, under OCV, SOFC and SOEC modes, indicating a better electrocatalytic activity for ORR than for OER. The accelerated electrochemical processes could be ascribed to

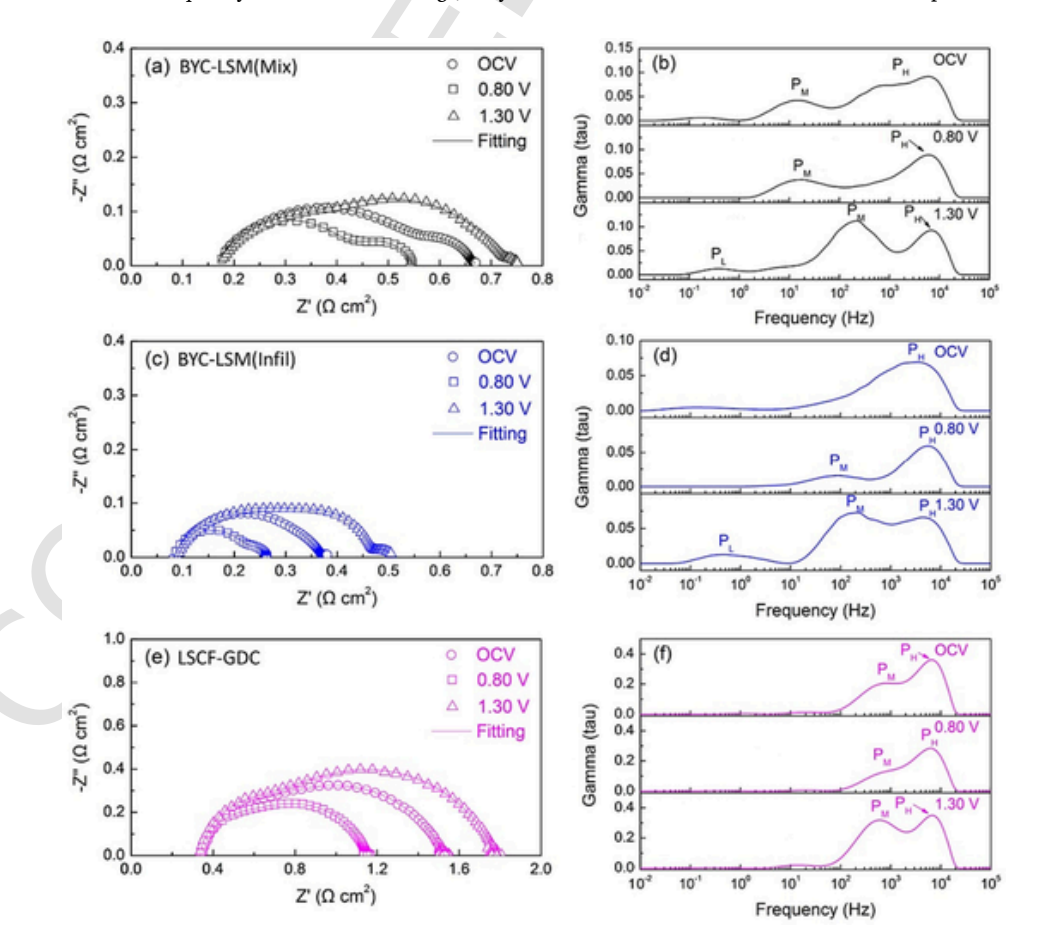


Fig. 4. Nyquist plots and the corresponding DRT profiles of the single cells with different OEs at 650 °C. (a) and (b): BYC-LSM(Mix), (c) and (d): BYC-LSM(Infil), and (e) and (f): LSCF-GDC. $H_2/H_2O = 50/50$.

Fig. 5. $R_{\rm ohm}$ and $R_{\rm p}$ of the three types of single cells under different operating conditions.

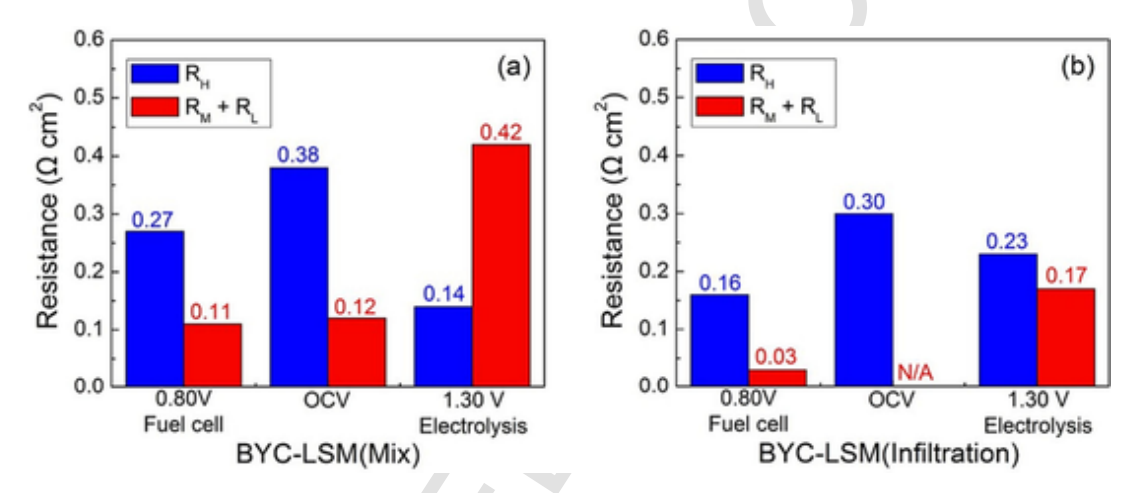


Fig. 6. $R_{\rm H}$ and $R_{\rm M}+R_{\rm L}$ of the single cells under different operating conditions.

the infiltrated LSM NPs and high oxide-ion conduction network, thus ensuring high TPB density and low charge transfer resistance ($R_{\rm H}$) [38,39]. Additionally, LSM NPs also increase specific surface area of the electrode, promoting surface oxygen exchange kinetics and reducing $R_{\rm M}$ + $R_{\rm L}$ [40].

Compared to the single cell employing the conventional LSCF-GDC OE with an additional GDC barrier layer and the same ScSZ electrolyte, the BYC-LSM(Mix) and BYC-LSM(Infil) cells exhibit significantly better performance (see Fig. 5). This is because significantly reduced $R_{\rm ohm}$ (by >50%) and $R_{\rm P}$ (59–75%) are achieved by the barrier layer-free OE consisting of highly oxide-ion and electron conductive phases, which increases TPB densities for fast ORR/OER kinetics. The results highlight the advantage of combining a fast oxide-ion conductor (BYC) and an excellent electronic conductor (LSM) to achieve high electrochemical activity for ORR/OER kinetics.

3.4. Electrode durability testing

The electrode durability was tested using single cells under cyclic operation conditions between fuel cell mode at 0.80 V and electrolysis mode at 1.30 V is shown in Fig. 7. For a single cell with BYC-LSM(Mix), Fig. 7(a) shows an initial discharging current density of 303 mA cm $^{-2}$ at 0.80 V in the fuel cell mode and 428 mA cm $^{-2}$ at 1.30 V in the electrolysis mode. During the 550-h operation, single cell exhibits a good performance stability with a low average degradation rate of 0.093–0.100 mA cm $^{-2}$ h $^{-1}$ in both fuel cell mode and electrolysis mode. The degradation rate is evidently lower than previously reported values on single cells employing LSCF-based OEs (e.g., degradation rate > 5% in 16 h), Nd₂NiO₄ Ruddlesden-Popper type OEs (degradation rate: 0.16 mA cm $^{-2}$ h $^{-1}$ in 500 h) and LSCF-GDC composite (degradation rate: 5.5 mA cm $^{-2}$ h $^{-1}$ in 60 h) [49] [3,6,50,51]. This comparison suggests that BYC-LSM is a better OE for RSOCs operated in either fuel cell or electrolysis mode.

For BYC-LSM(Infil) cell, Fig. 7(b) showed an average degradation rate of 0.120 mA cm⁻² h⁻¹ for both fuel cell and electrolysis mode, comparable to that of BYC-LSM(Mix) cell. However, the initial discharging current density and electrolysis current density was 1.5– 2 times higher, i.e., 575 and 694 mA cm⁻², respectively, than the BYC-LSM(Mix) cell. Thus, the degradation rate per 1000 h for the BYC-LSM (Infil) cell was 4.5%/kh and 2.7%/kh in the fuel cell mode and the electrolysis mode, respectively, which was significantly lower than the BYC-LSM(Mix) cell (degradation rate: 34%/kh in fuel cell mode and 34%/kh in electrolysis mode). This level of high performance is clearly the result of increased TPB density by using LSM NPs, oxide-ion conductive BYC, and stronger bonding between BYC phase and ScSZ electrolyte.

It is worth mentioning that both cells exhibited a faster degradation during fuel cell mode and an improvement during electrolysis mode in the first 10 h-cycle. The higher local steam content produced during fuel cell mode could be a reason for the subsequent higher electrolysis current density. Once steam concentration is stabilized in the following cycles, the cell current density is less affected, only showing generic degradation related to materials.

After the 550-h cyclic operation, electrochemical impedance spectra of single cells were measured under the OCV condition; the results are shown in Fig. 8. Ohmic and polarization resistance $R_{\rm p}$ extracted from the impedance spectra are listed in Table 2. The ohmic resistance of BYC-LSM(Mix) cell was increased from 0.17 to 0.22 Ω cm², while $R_{\rm p}$ was increased from 0.50 to 0.58 Ω cm². The increase of $R_{\rm p}$ is primarily attributed to the degradation of the electrochemical processes at the high-frequency impedance response (e.g., 10^3-10^4 Hz), which is related to charge transfer and supported by the partial delamination shown in later Fig. 9(a) of SEM images. In contrast, the BYC-LSM(Infil) cell exhibited a slight $R_{\rm ohm}$ increase from 0.07 to 0.09 Ω -cm², while $R_{\rm p}$ was only increased from 0.30 to 0.34 Ω -cm², which is also suggested by the intact interface in Fig. 9(b) of SEM image.

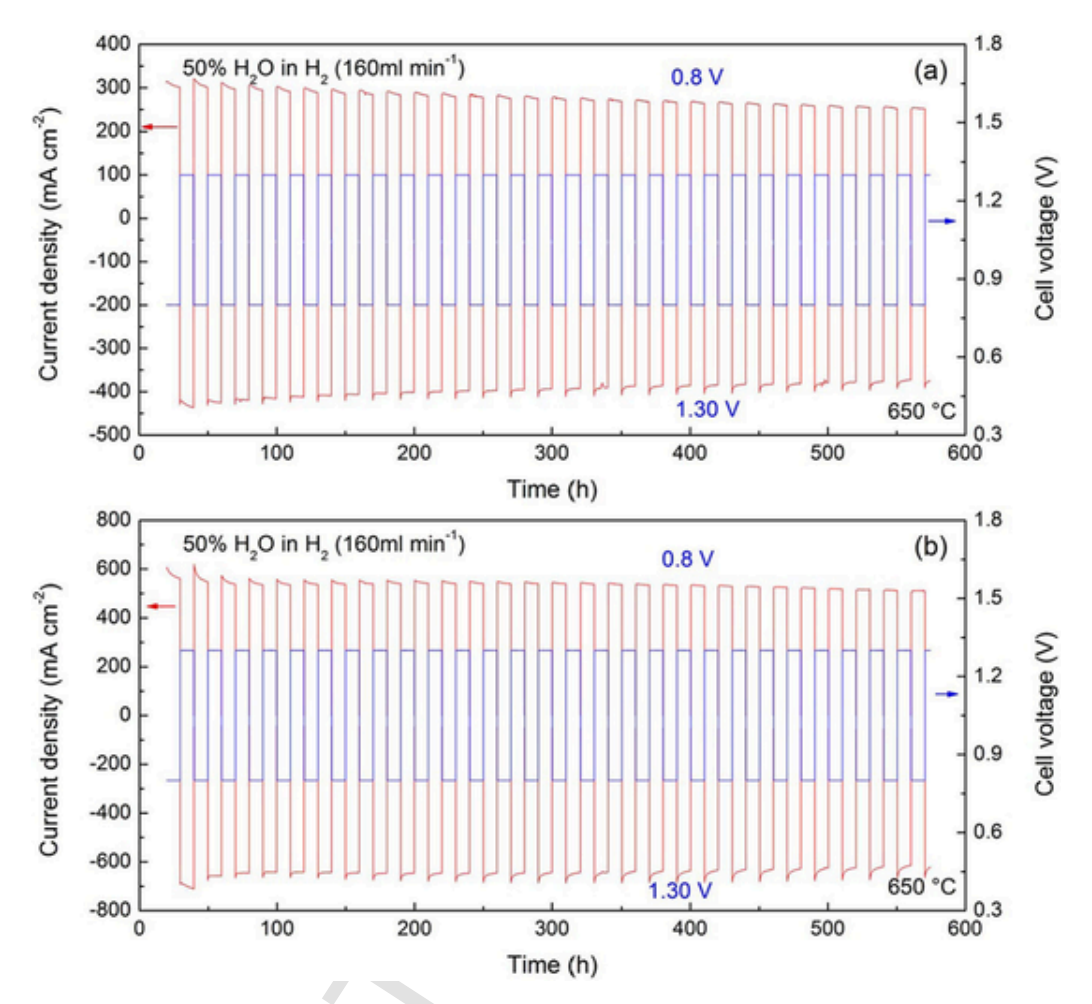


Fig. 7. Single cell durability testing with cycling from SOFC to SOEC mode at 650 °C: (a) BYC-LSM(Mix) oxygen electrode and (b) BYC-LSM(Infil) oxygen electrode.

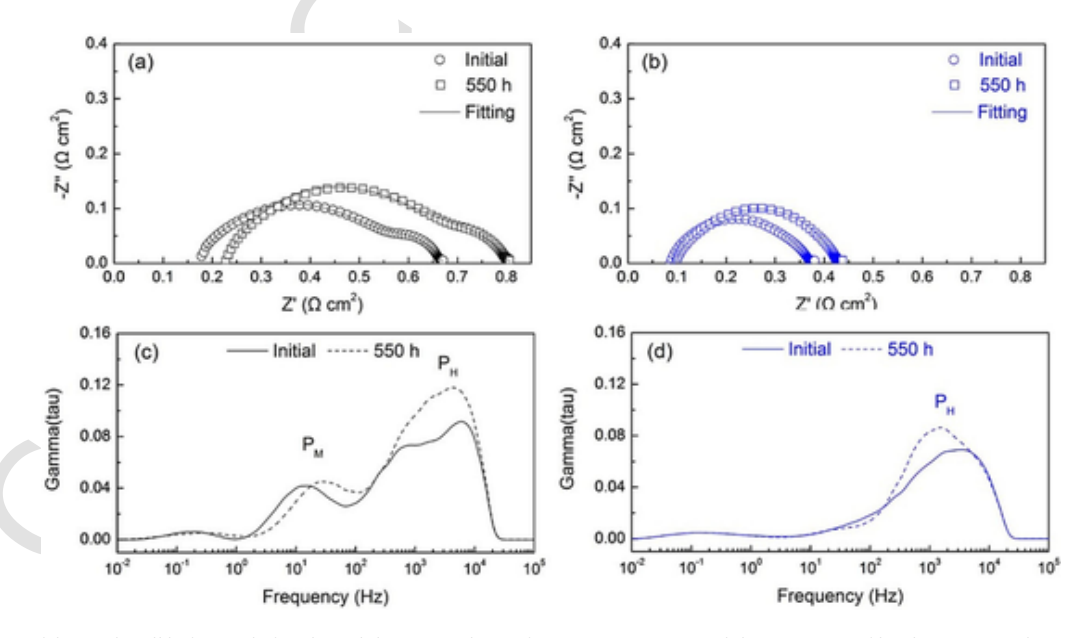


Fig. 8. Nyquist plots of the single cell before and after the stability test with OE of: (a) BYC-LSM(Mix) and (b) BYC-LSM(Infil). The corresponding DRT profiles: (c) BYC-LSM(Mix) and (d) BYC-LSM(Infil).

Fig. 9 of SEM examination on the tested sample reveals a partial delamination of BYC-LSM(Mix) from the electrolyte, which is responsible for the increased ohmic resistance. Moreover, partial coarsening of BYC and LSM particles (shown in Fig. 9 and compared to Fig. S9 in SI) has

been observed from the two cells, likely contributing to the increase of polarization resistance ($R_{\rm p}$). There also seems to be an enrichment of BYC phase at the interface. In comparison, the BYC-LSM(Infil) OE has a much better bonding with the electrolyte and a more uniform distribu-

Table 2Electrochemical parameters obtained from the impedance spectra of single cells before and after the performance stability testing.

Electrode	Condition	$R_{\rm ohm}$ (Ω cm ²)	R _H (Ω cm ²)	$R_{ m M}$ (Ω cm ²)	$R_{\rm p}$ (Ω cm ²)
BYC-LSM (Mix)	Initial	0.17	0.38	0.12	0.50
	550 h	0.22	0.40	0.18	0.58
BYC-LSM (Infil)	Initial	0.07	0.30	-	0.30
	550 h	0.09	0.34	-	0.34

tion of BYC and LSM phases without significant coarsening, which supports the observed lower $R_{\rm ohm}$ and $R_{\rm P}.$

4. Conclusions

A barrier layer free OE consisting of oxide-ion conducting BYC and electron-conducting LSM has been microstructurally and electrochemically evaluated for RSOCs in two forms: screen-printed (denoted as BYC-LSM(Mix)) and infiltrated (denoted as BYC-LSM(Infil)). Microstructurally, the latter is featured with LSM NPs decorating the BYC skeleton that is well bonded to the ScSZ electrolyte. These LSM NPs anchored on a highly oxide-ion conductive BYC backbone are responsible for the enhanced TPB density, increased surface oxygen exchange kinetics, and lowered polarization ASR (e.g., $0.1~\Omega\cdot\text{cm}^2$ at 650~°C). When used in a single cell operated at 650~°C, high current densities of $588~\text{mA}~\text{cm}^{-2}$ at 0.80~V and $688~\text{mA}~\text{cm}^{-2}$ at 1.30~V have been achieved with $50\%~\text{H}_2-50\%~\text{H}_2O$ at HE and air at OE. During a 550-h~SOFC/SOEC cyclic operation, a fairly stable performance with a moderately low degradation rate of $0.10~\text{m}~\text{A}~\text{cm}^{-2}~\text{h}^{-1}$ has been achieved. This level of performance is much better than the barrier layer present LSCF-GDC

cell. These results suggest that BYC-LSM(Infil) is a promising OE candidate for intermediate temperature RSOCs.

CR ediT authorship contribution statement

Kai Zhaα Writing – original draft, Methodology, Investigation, Formal analysis, Data curation. Jiaxin Lu: Methodology, Investigation. Long Le: Methodology, Investigation. Chris Coyle: Methodology, Investigation. Olga A. Marina: Writing – review & editing, Resources. Kevin Huang: Writing – review & editing, Supervision, Resources, Funding acquisition, Conceptualization.

Declaration of competing interest

This is to declare that all the authors of the submitted paper have no conflict of interest.

Data availability

Data will be made available on request.

Acknowledgments

This material is based upon work supported by the U.S. Department of Energy's Office of Energy Efficiency and Renewable Energy (EERE) under the Fuel Cell Technologies Office (FCTO) under Award Number DE-EE-0008842 and Office of Fossil Energy and Carbon Management under National Energy Technology Lab under award number DE-FE-32111. The authors would like to acknowledge J. Escobar at Pacific Northwest National Laboratory for performing SEM analyses.

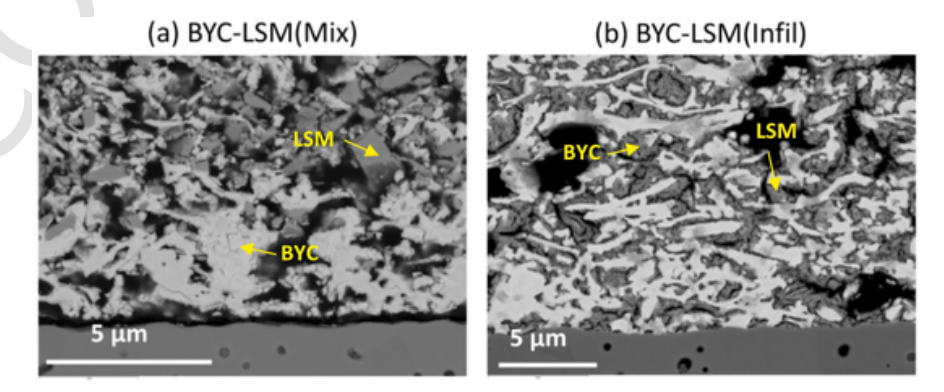


Fig. 9. SEM images of single cells with two types of BLF-OEs after the cyclic operation: (a) BYC-LSM(Mix) and (b) BYC-LSM(Infil).

Appendix A. Supplementary data

Supplementary data to this article can be found online at https://doi.org/10.1016/j.apenergy.2024.122962.

References

- Mogensen M.B. Materials for reversible solid oxide cells. Curr Opin Electrochem 2020;21:265–73. https://doi.org/10.1016/j.coelec.2020.03.014.
- [2] Min G, Choi S, Hong J. A review of solid oxide steam-electrolysis cell systems: thermodynamics and thermal integration. Appl Energy 2022;328:120145. https://doi.org/10.1016/j.apenergy.2022.120145.
- [3] Akter A, Mulligan J.R, Grande H, Pal U, Basu S.N, Gopalan S. Reversible solid oxide cells: early performance and microstructural evolution during electrolysis and switched mode operation. J Power Sources 2023;572:233093. https://doi.org/ 10.1016/j.jpowsour.2023.233093.
- [4] Khan M.S, Xu X, Knibbe R, Zhu Z. Air electrodes and related degradation mechanisms in solid oxide electrolysis and reversible solid oxide cells. Renew Sustain Energy Rev 2021;143:110918. https://doi.org/10.1016/ j.rser.2021.110918.
- [5] Liu Z, Han B, Lu Z, Guan W, Li Y, Song C, et al. Efficiency and stability of hydrogen production from seawater using solid oxide electrolysis cells. Appl Energy 2021;300:117439. https://doi.org/10.1016/j.apenergy.2021.117439.
- [6] Morales-Zapata M.A, Larrea A, Laguna-Bercero M.A. Reversible operation performance of microtubular solid oxide cells with a nickelate-based oxygen electrode. Int J Hydrogen Energy 2020;45:5535–42. https://doi.org/10.1016/ i.ilhydene.2019.05.122.
- [7] Zhang W, Zhou Y, Liu E, Ding Y, Luo Z, Li T, et al. A highly efficient and durable air electrode for intermediate-temperature reversible solid oxide cells. Appl Catal Environ 2021;299:120631. https://doi.org/10.1016/j.apcatb.2021.120631.
- [8] Aguadero A, Fawcett L, Taub S, Woolley R, Wu K.-T, Xu N, et al. Materials development for intermediate-temperature solid oxide electrochemical devices. J Mater Sci 2012;47:3925–48. https://doi.org/10.1007/s10853-011-6213-1.
- [9] Ahmad M.Z, Ahmad S.H, Chen R.S, Ismail A.F, Hazan R, Baharuddin N.A. Review on recent advancement in cathode material for lower and intermediate temperature solid oxide fuel cells application. Int J Hydrogen Energy 2022;47: 1103–20. https://doi.org/10.1016/j.jihydene.2021.10.094.
- [10] Shen J, Miao B, Liu Q, Wu Y, Chan S.H, Zhong Z, et al. Activation of LSCF-YSZ interface by cobalt migration during electrolysis operation in solid oxide electrolysis cells. Int J Hydrogen Energy 2022;47:38114–23. https://doi.org/10.1016/j.jihydene.2022.09.008.
- [11] Pan Z, Liu Q, Zhang L, Zhou J, Zhang C, Chan S.H. Experimental and thermodynamic study on the performance of water electrolysis by solid oxide electrolyzer cells with Nb-doped co-based perovskite anode. Appl Energy 2017; 191:559–67. https://doi.org/10.1016/j.apenergy.2017.01.090.
- [12] Shri Prakash B, Pavitra R, Senthil Kumar S, Aruna S.T. Electrolyte bi-layering strategy to improve the performance of an intermediate temperature solid oxide fuel cell: a review. J Power Sources 2018;381:136–55. https://doi.org/10.1016/ j.jpowsour.2018.02.003.
- [13] Li J, Fan L, Hou N, Zhao Y, Li Y. Solid oxide fuel cell with a spin-coated yttria stabilized zirconia/gadolinia doped ceria bi-layer electrolyte. RSC Adv 2022;12: 13220–7. https://doi.org/10.1039/d2ra02035a.
- [14] Zhang C, Huang K. A new composite cathode for intermediate temperature solid oxide fuel cells with zirconia-based electrolytes. J Power Sources 2017;342: 419.26 https://doi.org/10.1016/j.jrayeeur.2016.11.094.
- 419–26. https://doi.org/10.1016/j.jpowsour.2016.12.084.
 Zhang Y, Xu N, Tang Q, Huang K. Intermediate temperature solid oxide cell with a barrier layer free oxygen electrode and phase inversion derived hydrogen electrode. J Electrochem Soc 2022;169:034516. https://doi.org/10.1149/1945-7111/055652
- [16] Liu Y.L, Thydén K, Chen M, Hagen A. Microstructure degradation of LSM-YSZ cathode in SOFCs operated at various conditions. Solid State Ion 2012;206:97–103. https://doi.org/10.1016/j.ssi.2011.10.020.
- [17] Zhang M, Yang M, Hou Z, Dong Y, Cheng M. A bi-layered composite cathode of La_{0.8}Sr_{0.2}MnO₃-YSZ and La_{0.8}Sr_{0.2}MnO₃-La_{0.4}Ce_{0.6}O_{1.8} for IT-SOFCs. Electrochim Acta 2008;53:4998–5006. https://doi.org/10.1016/j.electacta.2008.01.095.
- [18] Huang K, Feng M, Goodenough J.B. Bi₂O₃ Y₂O₃ CeO₂ solid solution oxide-ion electrolyte. Solid State Ion 1996;89:17–24. https://doi.org/10.1016/0167-2738 (96)00260-3
- [19] Fang W, Yang T, Huang K. In situ synthesis of a high-performance bismuth oxide based composite cathode for low temperature solid oxide fuel cells. Chem Commun 2019;55:2801–4. https://doi.org/10.1039/c9cc00442d.
- [20] Wachsman E.D, Lee K.T. Lowering the temperature of solid oxide fuel cells. Science 2011;334:935–9. https://doi.org/10.1126/science.1204090.
- [21] Yun B.H, Kim K.J, Joh D.W, Chae M.S, Lee J.J, Kim D.W, et al. Highly active and durable double-doped bismuth oxide-based oxygen electrodes for reversible solid oxide cells at reduced temperatures. J Mater Chem A 2019;7:20558–66. https:// doi.org/10.1039/c9ta09203j.
- [22] Jiang Z, Zhang L, Cai L, Xia C. Bismuth oxide-coated (La,Sr)MnO₃ cathodes for intermediate temperature solid oxide fuel cells with yttria-stabilized zirconia electrolytes. Electrochim Acta 2009;54:3059–65. https://doi.org/10.1016/ j.electacta.2008.11.067.
- [23] Lee K.T, Jung D.W, Yoon H.S, Lidie A.A, Camaratta M.A, Wachsman E.D. Interfacial modification of La_{0.8}0Sr_{0.2}0MnO_{3.8}-Er_{0.4}Bi_{0.6}O₃ cathodes for high performance lower temperature solid oxide fuel cells. J Power Sources 2012;220:

- 324-30. https://doi.org/10.1016/j.jpowsour.2012.08.004.
- [24] Yan J, Zhao Z, Shang L, Ou D, Cheng M. Co-synthesized Y-stabilized Bi₂O₃ and Sr-substituted LaMnO₃ composite anode for high performance solid oxide electrolysis cell. J Power Sources 2016;319:124–30. https://doi.org/10.1016/j.jpowsour.2016.04.042.
- [25] Park J.W, Lee K.T. Enhancing performance of La_{0.8}Sr_{0.2}MnO_{3.6}-infiltrated Er_{0.4}Bi_{1.6}O₃ cathodes via controlling wettability and catalyst loading of the precursor solution for IT-SOFCs. J Ind Eng Chem 2018;60:505–12. https://doi.org/ 10.1016/j.jiec.2017.11.039.
- [26] Zhao E, Liu X, Liu L, Huo H, Xiong Y. Effect of $La_{0.8}Sr_{0.2}Co_{0.2}Fe_{0.8}O_{3.6}$ morphology on the performance of composite cathodes. Prog Nat Sci Mater 2014;24:24–30. https://doi.org/10.1016/j.pnsc.2014.01.008.
- [27] Wang J, Zhao K, Zhao J, Li J, Liu Y, Chen D, et al. A NiMo-YSZ catalyst support layer for regenerable solid oxide fuel cells running on isooctane. Appl Energy 2022; 326:119907. https://doi.org/10.1016/j.apenergy.2022.119907.
- [28] Meng X, Liu Y, Yang N, Tan X, Liu J, Diniz da Costa J.C, et al. Highly compact and robust hollow fiber solid oxide cells for flexible power generation and gas production. Appl Energy 2017;205:741–8. https://doi.org/10.1016/ j.apenergy.2017.08.109.
- [29] Khan M.Z, Mehran M.T, Song R.H, Lee J.W, Lee S.B, Lim T.H. A simplified approach to predict performance degradation of a solid oxide fuel cell anode. J Power Sources 2018;391:94–105. https://doi.org/10.1016/ j.jpowsour.2018.04.080.
- [30] Liu Q, Dong X, Xiao G, Zhao F, Chen F. A novel electrode material for symmetrical SOFCs. Adv Mater 2010;22:5478–82. https://doi.org/10.1002/ adma.201001044.
- [31] Wan T.H, Saccoccio M, Chen C, Ciucci F. Influence of the discretization methods on the distribution of relaxation times deconvolution: implementing radial basis functions with DRTtools. Electrochim Acta 2015;184:483–99. https://doi.org/ 10.1016/j.electacta.2015.09.097.
- [32] Osinkin D.A. Detailed analysis of electrochemical behavior of high-performance solid oxide fuel cell using DRT technique. J Power Sources 2022;527:231120. https://doi.org/10.1016/j.jpowsour.2022.231120.
- [33] Li H, Wei W, Liu F, Xu X, Li Z, Liu Z. Identification of internal polarization dynamics for solid oxide fuel cells investigated by electrochemical impedance spectroscopy and distribution of relaxation times. Energy 2023;267:126482. https://doi.org/10.1016/j.energy.2022.126482.
- [34] Ramos T, Søgaard M, Mogensen M.B. Electrochemical characterization of Ni/ ScYSZ electrodes as SOFC anodes. J Electrochem Soc 2014;161:F434. https:// doi.org/10.1149/2.045404jes.
- [35] Lin Y, Zhou W, Sunarso J, Ran R, Shao Z. Characterization and evaluation of BaCo_{0.7}Fe_{0.2}Nb_{0.1}O_{3.5} as a cathode for proton-conducting solid oxide fuel cells. Int J Hydrogen Energy 2012;37:484–97. https://doi.org/10.1016/ j.ijhydene.2011.09.010.
- [36] Hou J, Zhu Z, Qian J, Liu W. A new cobalt-free proton-blocking composite cathode La₂NiO_{4+x}-LaNl_{0.6}Fe_{0.4}O_{3.5} for BaZr_{0.1}Ce_{0.7}Y_{0.2}O_{3.5}-based solid oxide fuel cells. J Power Sources 2014;264:67–75. https://doi.org/10.1016/ j.jpowsour.2014.04.089.
- [37] Plonczak P, Sørensen D.R, Søgaard M, Esposito V, Hendriksen P.V. Electrochemical properties of dense (La, Sr)MnO_{3-δ} films produced by pulsed laser deposition. Solid State Ion 2012;217:54–61. https://doi.org/10.1016/ j.ssi.2012.03.043.
- [38] Lou X, Wang S, Liu Z, Yang L, Liu M. Improving $La_{0.6}Sr_{0.4}Co_{0.2}Fe_{0.8}O_{3.\delta}$ cathode performance by infiltration of a $Sm_{0.5}Sr_{0.5}CoO_{3.\delta}$ coating. Solid State Ion 2009;180: 1285–9. https://doi.org/10.1016/j.ssi.2009.06.014.
- [39] Ding D, Li X, Lai S.Y, Gerdes K, Liu M. Enhancing SOFC cathode performance by surface modification through infiltration. Energ Environ Sci 2013;7:552–75. https://doi.org/10.1039/c3ee42926a.
- [40] Liu M, Ding D, Blinn K, Li X, Nie L, Liu M. Enhanced performance of LSCF cathode through surface modification. Int J Hydrogen Energy 2012;37:8613–20. https://doi.org/10.1016/j.ijhydene.2012.02.139.
- [41] Sındıraç C, Büyükaksoy A, Akkurt S. Electrochemical performance of $\begin{array}{lll} La_{0,6}Sr_{0,4}Co_{0,2}Fe_{0,8}O_{3}-Ce_{0,9}Gd_{0,1}O_{2,\delta} & composite SOFC & cathodes fabricated by \\ electrocatalyst & and/or electrocatalyst-ionic conductor infiltration. J Sol-Gel Sci Technol 2019;92:45–56. https://doi.org/10.1007/s10971-019-05073-5. \end{array}$
- [42] Pan W, Chen K, Ai N, Lü Z, Jiang S.P. Mechanism and kinetics of Ni-Y₂O₃-ZrO₂ hydrogen electrode for water electrolysis reactions in solid oxide electrolysis cells. J Electrochem Soc 2016;163:F106. https://doi.org/10.1149/2.0801602jes.
- [43] Lee Y.H, Lee S, Zeng J, Cha S.W, Chang I. Au-coated lanthanum strontium cobalt ferrite cathode for lowering sheet resistance of a solid oxide fuel cell. Int J Precis Eng Man 2019;20:451–5. https://doi.org/10.1007/s12541-019-00013-3.
- [44] Zhao K, Kim B.H, Norton M.G, Ha S.Y. Cathode optimization for an inert-substrate-supported tubular solid oxide fuel cell. Front Energy Res 2018;6. https://doi.org/10.3389/fenrg.2018.00087.
- [45] Zheng Z, Jing J, Lei Z, Wang Z, Yang Z, Jin C, et al. Performance and DRT analysis of infiltrated functional cathode based on the anode supported SOFCs with long-term stability. Int J Hydrogen Energy 2022;47:18139–47. https://doi.org/10.1016/j.ijhydene.2022.03.289.
- [46] Chen S, Gu D, Zheng Y, Chen H, Guo L. Enhanced performance of NiO-YSZ planar anode-supported SOFC with an anode functional layer. J Mater Sci 2020;55:88–98. https://doi.org/10.1007/s10853-019-04007-4.
- [47] Zapata-Ramírez V, Mather G.C, Azcondo M.T, Amador U, Pérez-Coll D. Electrical and electrochemical properties of the Sr(Fe,Co,Mo)O₃₋₅ system as air electrode for reversible solid oxide cells. J Power Sources 2019;437:226895. https://doi.org/ 10.1016/j.jpowsour.2019.226895.
- 48] Brisse A, Schefold J, Zahid M. High temperature water electrolysis in solid oxide

- cells. Int J Hydrogen Energy 2008;33:5375–82. https://doi.org/10.1016/j.ijhydene.2008.07.120.
- [49] Park J.H, Jung C.H, Kim K.J, Kim D, Shin H.R, Hong J.E, et al. Enhancing bifunctional electrocatalytic activities of oxygen electrodes via incorporating highly conductive Sm³⁺ and Nd³⁺ double-doped ceria for reversible solid oxide cells. ACS Appl Mater Interfaces 2021;13:2496–506. https://doi.org/10.1021/ acsami.0c17238.
- [50] Fan H, Keane M, Li N, Tang D, Singh P, Han M. Electrochemical stability of $\rm La_{0.6}Sr_{0.4}Co_{0.2}Fe_{0.8}O_{3.6}\text{-}infiltrated YSZ oxygen electrode for reversible solid oxide}$
- fuel cells. Int J Hydrogen Energy 2014;39:14071–8. https://doi.org/10.1016/j.ijhydene.2014.05.149.
 [51] Liu Y, Tian Y, Wang Y, Li Y, Pu J, Ciucci F, et al. Nano film Pr₂Ni_{0.8}Cu_{0.2}O_{4+δ} decorated La_{0.6}Sr_{0.4}Co_{0.2}Fe_{0.8}O_{3-δ} oxygen electrode for highly efficient and stable reversible solid oxide cells. Electrochim Acta 2022;430:141032. https://doi.org/10.1016/final.com/14.0007 10.1016/j.electacta.2022.141032.

